



Plasmonics-based gas sensor with photonic spin hall effect in broad terahertz frequency range under variable chemical potential of graphene

Anuj K. Sharma¹ · Parmod Kumar¹ · Yogendra Kumar Prajapati²

Received: 24 November 2021 / Accepted: 22 February 2022 / Published online: 12 May 2022

© The Author(s), under exclusive licence to Springer Science+Business Media, LLC, part of Springer Nature 2022

Abstract

Graphene monolayer of sub-nanometer thickness possesses strong metallic and plasmonic behavior in a broad terahertz (THz) frequency range. This plasmonic effect can be considerably manipulated when graphene layer is subjected to a variable chemical potential (E_f) via chemical doping or electrical gating. The strong adsorption characteristics of graphene layer is another important advantage. In this work, a photonic spin Hall effect (PSHE) based plasmonic sensor consisting of germanium prism, organic dielectric layer, and graphene monolayer is simulated and analyzed in THz range aiming at highly sensitive and reliable gas sensing. Modified Otto configuration and Kubo formulation for graphene at room temperature are considered. The sensor's performance is examined in terms of figure of merit (FOM). The analysis indicates that under angular interrogation scheme of sensor operation, the FOM improves for smaller chemical potential (moderate doping) and higher THz frequency. Moreover, the influence of temperature on gas sensor's performance (FOM) is negligible, which suggests that the sensor is capable of providing stable sensing performance against temperature variation. The sensor design is highly flexible in terms of selection of THz frequency as an alternative interrogation scheme (*i.e.*, measuring the variation in spin-dependent shift peak value of PSHE spectrum upon change in gas medium refractive index) can also be implemented. It is found that there is no need to change the moderate doping of graphene monolayer (*i.e.*, E_f remains around its normal value ~ 0.1 eV) as the sensitivity achievable with this alternative method has considerably greater magnitude at smaller THz frequency (*e.g.*, 2 THz). The magnitudes of FOM (with angular interrogation method) and sensitivity (with alternative method) are found to be significantly greater for rarer gaseous media, which might possibly assist in early detection of airborne viruses such as SARS-Cov-2 (while using appropriate specificity method) and to measure the concentration of a particular gas in a given gaseous mixture.

Keywords Terahertz · Graphene · Chemical potential · Plasmon · Photonic spin hall effect · Gas sensor

✉ Anuj K. Sharma
anujsharma@nitdelhi.ac.in

¹ Physics Division, Department of Applied Sciences, National Institute of Technology (NIT) Delhi, GT Karnal Road, Delhi 110036, India

² ECE Department, MNNIT Allahabad, Prayagraj, Uttar Pradesh, India

1 Introduction

Spin hall effect (SHE) refers to the splitting of spin up and spin down electrons inducing spin current perpendicular to the direction of applied electric field (Kato et al. 2004; Hirsch 1999). Photonic Spin Hall Effect (PSHE) has been attracting a lot of attention in magneto-optical effects (Rizal 2021; Liu 2019). PSHE is the optical analogy of SHE where spin photon plays the role of spin electron and the electric field is replaced by refractive index (RI) gradient (Bliokh and Bliokh 2004; Aiello and Woerdman 2008). The reason for the PSHE is credited to a spin-orbital interaction between spin polarization and trajectory of light is the origin of PSHE (Liu 2019; Ling 2017; Murakami et al. 2003). PSHE is referred to as the displacement normal to the plane of incidence corresponding to the splitting of left or right circularly polarized component when the beam is reflected or transmitted through a plane interface (Bliokh et al. 2015; Gosselin and Be 2007).

PSHE has become a potential candidate for finding applications in different research areas including plasmonics (Filonov et al. 2014; Ling et al. 2012). PSHE has been utilized to calculate the optical thickness of nanostructures (Boucaud et al. 2014), and to identify graphene layers (Zhou 2012). It has also been implemented to investigate more complicated configurations and materials such as left-handed materials and photonic tunneling (Zhou et al. 2014).

Spin-dependent splitting (SDS) corresponding to PSHE is small in magnitude so a few methods have been proposed to enhance the SDS (Prajapati 2021). PSHE enabled surface plasmon resonance (SPR)-based sensors are strong candidates for enhanced SDS (Xiang et al. 2017; Srivastava et al. 2021). PSHE enhancement was reported by considering SPR effect in a three-layer structure composed of glass, metal, and air (Srivastava et al. 2021). It was found that a horizontal polarization beam can be used to excite SPR, leading to a significant transverse SDS far greater than the previous reported results observed at the air-glass interface. Another study reported an enhancement of PSHE by using long-range SPR (LRSPR) (Tan and Zhu 2016).

From the above studies, one can establish that SDS can be improved by utilizing the SPR effect. It is known that SPR sensors possess high sensitivity and reliability, that lead them to find a large number of applications in bio- and chemical sensors including biomolecular interaction. The SPR sensors generally operate in visible and infrared (IR) range with noble metals such as gold and silver (Sharma and Nagao 2014). There has recently been considerable research work on SPR-based and localized SPR-based sensors for biomedical detection (Lobry et al. 2020; Kumar et al. 2021). Research of SPR sensors in the terahertz (THz) range is relatively moderate as surface plasmon polaritons (SPPs) are found to be extremely unconfined (known as Zenneck waves) (Barlow and Cullen 1953). This unconfined nature of SPPs leads to limit the performance of SPR-based sensors in THz. At the same time, a large number of molecules contain their collective rotational and vibrational modes in THz frequency range, therefore, SPR-based sensors need to be explored in great detail in THz frequency range. In order to tackle the above issue of poor confinement of SPPs in THz, many artificially engineered structures have been proposed such as Sievenpiper mushrooms and periodic patches (Lockyear et al. 2009; Yao and Zhong 2014), tunable SP-like modes supported on metal surfaces corrugated with nano-holes or nanorods (Pendry et al. 2004), hollow square-ended brass tubes (Hibbins et al. 2005), and periodically perforated metallic plates (Ulrich and Tacke 1973). But all these modifications result in bulky size and a complex design of SPR sensor. In most of those cases, the SPPs confinement is not that good either.

Graphene, a 2D form of carbon having atoms arranged in honeycomb lattice, is looked at as a suitable alternative to noble plasmon-active metals (e.g., Ag, Au etc.) in THz as it has the capability to support surface plasmon wave (SPW) at very low Fermi energy level owing to its negative imaginary part of conductivity in THz frequency range (Bao and Loh 2012). Highly doped graphene monolayer has been used for SP excitation at terahertz frequencies (Gan 2012; Novoselov et al. 2004). Graphene-based SPPs have larger confinement and have relatively long propagation distances in THz, while possessing the advantage of being highly tunable via electrical and chemical doping methods (Koppens et al. 2011; Gan et al. 2012). Recently, graphene-based SPR sensor at five terahertz had been reported (Zhang, et al. 2017a).

In this paper, we have reported an enhanced PSHE-enabled gas sensor with graphene monolayer in a broad THz frequency region (2–10 THz). Modified Otto configuration has been used. Germanium (Ge) is used as light coupling prism, which assists in momentum matching between SPW and incident p-polarized THz radiation. Further, the influence of graphene’s variable chemical potential and temperature on gas sensor’s performance is examined and analyzed in a broad frequency region (2–10 THz). Both angular interrogation and SDS magnitude interrogation methods are explored while analyzing the gas sensor’s performance.

2 Graphene’s optical properties in THz and Pshe-based sensor design

(i) Graphene’s optical properties in THz under the variation of chemical potential.

The frequency (ν), chemical potential (E_f), and temperature-dependent dielectric constant of graphene is considered which has already been studied (Jabbarzadeh et al. 2019). The two-dimensional conductivity of Graphene has a complex value, which consists of interband and intraband conductivities, and its value is dependent on the energy of incident radiation. The two-dimensional conductivity of graphene, which is extracted from Kubo formulation (Aliofkhazraei et al. 2016), is defined by the following relation:

$$\sigma_{intra} = \frac{ie^2k_B T}{\pi\hbar^2(\omega + i\tau^{-1})} \left[\frac{E_f}{k_B T} + 2\ln\left(\exp\left(\frac{-E_f}{k_B T}\right) + 1\right) \right] \tag{1}$$

$$\sigma_{inter} = \frac{ie^2}{4\pi\hbar} \ln \left[\frac{2|E_f| - (\omega + i\tau^{-1})\hbar}{2|E_f| - (\omega + i\tau^{-1})\hbar} \right] \tag{2}$$

$$\tau = \frac{\mu E_f}{eV_f^2} \tag{3}$$

In above expressions, $e, \omega (= 2\pi\nu), E_f, \hbar, T, \tau, \mu,$ and v_f are the electron charge, angular frequency of THz radiation, chemical potential (or Fermi energy), reduced Planck’s constant, temperature, electron relaxation time, carrier mobility in graphene, and Fermi velocity in graphene, respectively. Net optical conductivity (σ) of graphene is the sum of its intraband and interband contributions:

$$\sigma = \sigma_{intra} + \sigma_{inter} \tag{4}$$

Following the calculation of conductivity, the complex relative permittivity (ϵ_g) of graphene monolayer is computed from the following expression:

$$\epsilon_g = 1 + \frac{i\sigma}{\omega\epsilon_0 t} \tag{5}$$

In Eq. (5), $t=0.34$ nm is the effective thickness of graphene monolayer, and $\epsilon_0=8.854 \times 10^{-12}$ F/m is the permittivity of vacuum. Further, $\mu=1$ m²/(Vs) and $v_F=9.5 \times 10^5$ m/s for graphene. Similar formulations for studying graphene’s dielectric function (ϵ_g) have been used in previous studies also which assert that in the frequency range of 1–10 THz, the real part of ϵ_g is negative while its imaginary part is positive (Li et al. 2017). Also, the absolute value of ϵ_g increases as chemical potential increases. It is worth-mentioning that there are two types of chemical doping: surface transfer and substitutional doping. In the substitutional doping, some of carbon atoms in the graphene lattice are substituted by other atoms (*e.g.*, boron and nitrogen) with a different number of valence electrons. The surface transfer doping is primarily non-destructive and takes place owing to transfer of charge between graphene and surface adsorbates (Pinto and Markevich 2014).

(ii) **Graphene-based sensor design with PSHE in THz.**

Schematic of the 4-layer PSHE based plasmonic sensor probe is shown in Fig. 1.

Modified Otto configuration is used where Ge prism (RI= n_1) and graphene monolayer (RI= $n_3 = \sqrt{\epsilon_g}$ and thickness $d_3=t=0.34$ nm) are separated by a dielectric organic layer (RI= n_2 and thickness $d_2=12$ μ m) (Otto 1968; Srivastava et al. 2016). The typical values of n_1 (=4) and n_2 (=1.5) at 5 THz are taken as averaged ones in the corresponding frequency range of 2–10 THz (Zhang, et al. 2017a). Further, temperature-dependent variation in RI of Ge is considered (Naftaly et al. 2021). The thermo-optic effect in organic layer can be approximated by the same in silica. The possible alternatives of Ge substrate may be high-index chalcogenide glasses (such as 2S2G, As₂S₃ etc.). In order to calculate the transverse SDS, a general beam propagation model using angular spectrum theory is employed with an incident beam of Gaussian form:

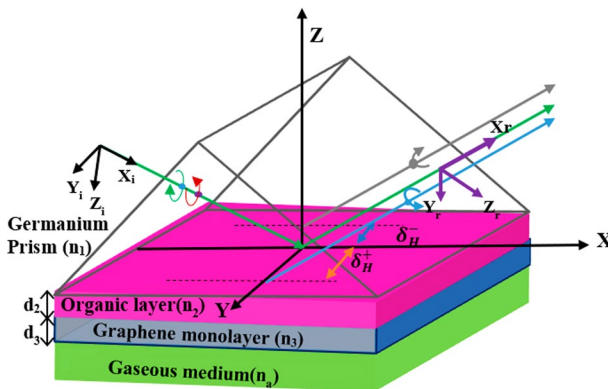


Fig. 1 Schematic diagram of 4-layer PSHE based plasmonic sensor. Graphene monolayer is considered to be under the variable chemical potential

$$\tilde{E}_i = \frac{\omega_0}{\sqrt{2\pi}} \exp\left[-\omega_0^2(k_{ix}^2 + k_{iy}^2)/4\right] \tag{6}$$

In Eq. (6), ω_0 is the beam waist, and k_{ix} and k_{iy} are the wave vector components in x_i and y_i directions, respectively. In the spin basis set, the incident beam can be written as:

$$\tilde{E}_i^H = (\tilde{E}_{i+} + \tilde{E}_{i-})/\sqrt{2} \tag{7}$$

$$\tilde{E}_i^V = i(\tilde{E}_{i-} - \tilde{E}_{i+})/\sqrt{2} \tag{8}$$

Here, H and V stand for horizontal and vertical polarization states, respectively. Further, \tilde{E}_{i+} And \tilde{E}_{i-} denote the left and right-handed circularly polarized components, respectively. Transverse displacement of the decomposed H and V polarization incidence (Zhou et al. 2014), respectively, can be written as:

$$\delta_H^\pm = \mp \frac{k_0 \omega_0^2 \left(1 + |r_s|/|r_p|\right) \cot \theta}{k_0^2 \omega_0^2 + \left|\frac{\partial \ln r_p}{\partial \theta_i}\right| + \left|\left(1 + \frac{r_s}{r_p}\right) \cot \theta\right|^2} \tag{9}$$

$$\delta_V^\pm = \mp \frac{k_0 \omega_0^2 \left(1 + |r_p|/|r_s|\right) \cot \theta}{k_0^2 \omega_0^2 + \left|\frac{\partial \ln r_s}{\partial \theta_i}\right| + \left|\left(1 + \frac{r_p}{r_s}\right) \cot \theta\right|^2} \tag{10}$$

If the reflection coefficients r_p (p-polarization) and r_s (s-polarization) are insensitive to θ , the above expressions can be simplified by considering the zero-order Taylor series (Xiang et al. 2017):

$$\delta_H^\pm = \mp \left(1 + |r_s|/|r_p|\right) \cot \theta / k_0 \tag{11}$$

$$\delta_V^\pm = \mp \left(1 + |r_p|/|r_s|\right) \cot \theta / k_0 \tag{12}$$

It should be noted that r_p and r_s for the proposed 4-layer sensor model can be calculated using transfer matrix method (Hetch 2002). MATLAB is used for the simulation of PSHE based sensor’s performance. From Eqs. (11–12), it is clear that δ_H components will be significantly greater than δ_V ones. Hence, the proposed sensor will be evaluated by considering δ_H only.

3 Results and discussion

(i) PSHE based plasmonic probe with angular interrogation for gas sensing in THz

Figure 2 depicts the simulated PSHE curves (*i.e.*, the angular variation of δ_H^-) for different gaseous medium RI (n_a) values ranging between 1 and 1.1 while three figures representing the PSHE curves for different sets of (ν , E_p) as (a) (2 THz, 0.1 eV), (b) (10 THz, 0.1 eV), and (c) (10 THz, 0.6 eV). The value of angle (θ) where a given PSHE spectrum

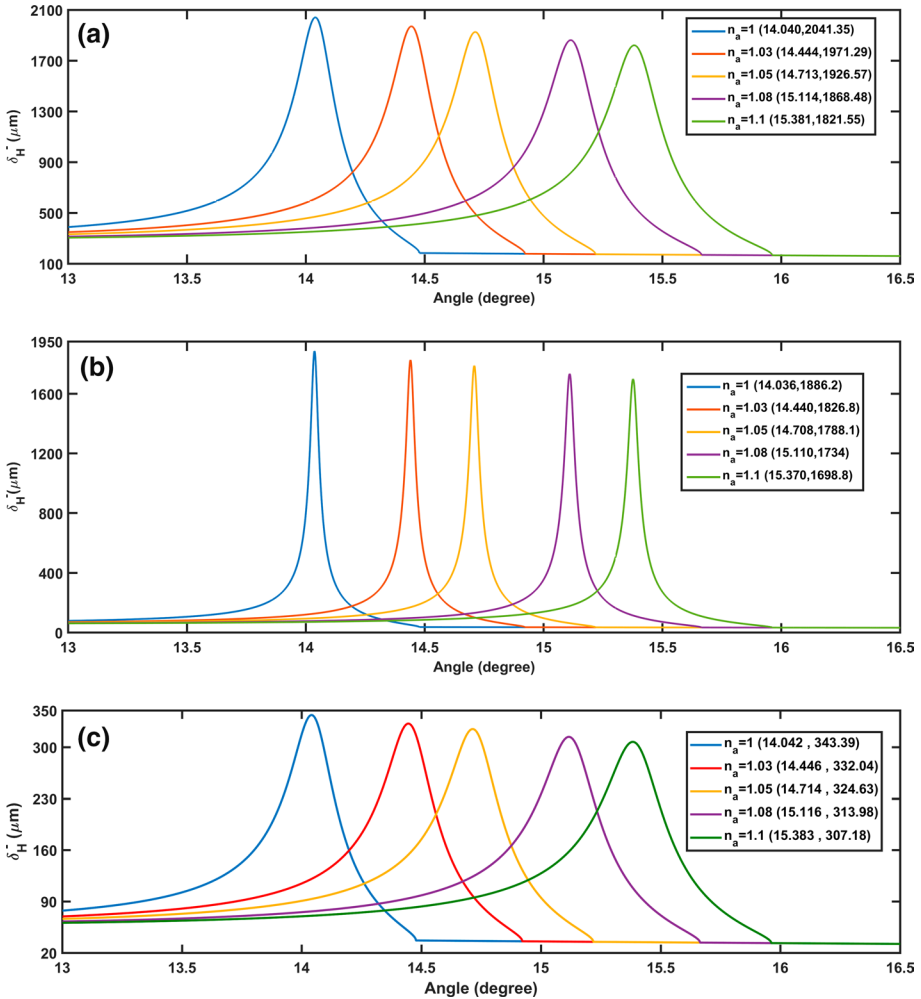


Fig. 2 Simulated angular variation of δ_H^- (i.e., PSHE spectrum) for different n_a values corresponding to **a.** $\nu=2$ THz and $E_f=0.1$ eV, **b.** $\nu=10$ THz and $E_f=0.1$ eV, and **c.** $\nu=10$ THz and $E_f=0.6$ eV. The corresponding values of peak SDS (δ_H^-) and θ_{SPR} are also mentioned in all three figures

(corresponding to a particular n_a value) achieves a peak value is known as the resonance angle (designated as θ_{SPR}).

Clearly, **(a)** and **(b)** parts of above figure enable to appreciate the difference among PSHE spectra for two different frequencies (2 THz and 10 THz) at a common chemical potential (0.1 eV) of graphene. Whereas, **(b)** and **(c)** parts lead to appreciate the difference among PSHE spectra for two different chemical potential values (0.1 eV and 0.6 eV) at a common frequency (10 THz). From Fig. 2a and b, it can be observed that PSHE spectrum for any given value of n_a undergoes a considerable variation (in terms of θ_{SPR} , peak SDS value, and width of PSHE curve) when the radiation frequency is changed (from 2 to 10 THz in this case). For instance, at $n_a=1$, θ_{SPR} changes from 14.040° (for $\nu=2$ THz) to 14.036° (for $\nu=10$ THz). Similarly, at $n_a=1.1$, θ_{SPR} changes from 15.381° (for $\nu=2$ THz) to 15.370° (for $\nu=10$ THz). Analyzing it even more minutely, the value of θ_{SPR} changes

merely by 0.004° for $n_a=1$ and 0.011° for $n_a=1.1$ corresponding to a significantly large variation in ν (*i.e.*, $\Delta\nu=8$ THz). The above values suggest that the ν -dependent variation in θ_{SPR} is very slow. However, the same may not be the case with SDS peak magnitude. From Fig. 2a and b, it can be observed that at $n_a=1$, SDS peak value changes from $2041.35 \mu\text{m}$ (for $\nu=2$ THz) to $1886.2 \mu\text{m}$ (for $\nu=10$ THz). Similarly, at $n_a=1.1$, SDS peak value changes from $1821.55 \mu\text{m}$ (for $\nu=2$ THz) to $1698.80 \mu\text{m}$ (for $\nu=10$ THz). A closer analysis reveals that the peak SDS value changes significantly by $219.80 \mu\text{m}$ for $n_a=1$ and $122.75 \mu\text{m}$ for $n_a=1.1$ corresponding to $\Delta\nu=8$ THz. These values clearly suggest that, unlike θ_{SPR} , peak SDS magnitude has stronger dependence on ν .

From Fig. 2b and c, it can be observed that PSHE spectrum for any given value of n_a undergoes a considerable variation when the chemical potential is changed (from 0.1 eV to 0.6 eV in this case). It is evident from the corresponding values of θ_{SPR} mentioned in Fig. 2b and c that the E_f -dependent variation in θ_{SPR} is very slow as the value of θ_{SPR} changes merely by 0.006° for $n_a=1$ and 0.013° for $n_a=1.1$ corresponding to a significantly large variation in E_f (*i.e.*, $\Delta E_f=0.5$ eV). However, the effect of E_f variation on SDS peak value is extremely large. From Fig. 2b and c, it can be observed that at $n_a=1$, SDS peak value changes from $1886.2 \mu\text{m}$ (for $E_f=0.1$ eV) to $343.39 \mu\text{m}$ (for $E_f=0.6$ eV). Similarly, at $n_a=1.1$, SDS peak value changes from $1698.80 \mu\text{m}$ (for $E_f=0.1$ eV) to $307.18 \mu\text{m}$ (for $E_f=0.6$ eV). A closer analysis reveals that the peak SDS value changes significantly by $1542.81 \mu\text{m}$ for $n_a=1$ and $1391.62 \mu\text{m}$ for $n_a=1.1$ corresponding to $\Delta E_f=0.5$ eV.

The above discussion indicates towards the important role of ν and E_f on proposed sensor's output characteristics. Importantly, it should be appreciated that the above ν - and E_f -dependent deviations in SDS and θ_{SPR} will, respectively, affect the detection accuracy (that depends on PSHE curve width) and sensitivity. At this point, it is worth-mentioning that the sensor's overall performance is evaluated in terms of figure-of-merit (FOM):

$$FOM(RIU^{-1}) = \frac{\delta\theta_{SPR}}{\delta n_a \times FWHM} \tag{13}$$

In Eq. (13), $\delta\theta_{SPR}$ is the angular shift of PSHE curve peak corresponding to δn_a variation in gaseous medium RI, and FWHM is the angular width of PSHE spectrum. FOM consists of two individual performance components, *i.e.*, sensitivity ($S_a = \frac{\Delta\theta_{SPR}}{\Delta n_a}$ in deg./RIU), and accuracy $A = 1/FWHM$ in deg.⁻¹). The unit of FOM is RIU^{-1} from Eq. (13). In the next section, a combined effect of ν and E_f on proposed sensor's FOM is analyzed in detail.

(ii) Coupled effect of THz frequency and graphene's chemical potential on PSHE-based gas sensor's FOM

Figure 3 presents the 2D (ν - E_f) variation of FOM of the proposed gas sensor.

The radiation frequency has been varied between 2 and 10 THz for above plot, and the chemical potential of graphene has been considered between 0.1 eV and 1.1 eV. While the upper limit (1.1 eV) of chemical potential represents the higher doping, the lower limit (0.1 eV) represents the moderate doping of graphene. In line with the discussion related to Fig. 2, the 2D variation in Fig. 3 demonstrates that the proposed sensor's FOM achieves the highest value for greater THz frequency and smaller chemical potential. It is important to note that while the smaller chemical potential is convenient from the sensor fabrication viewpoint, opting for radiation frequency greater than 10 THz may not be appropriate as many critical gas sensing applications (*e.g.*, for toxic gases such as hydrogen sulfide, sulfur hexafluoride, carbon disulphide etc.) are limited in the vicinity of 10 THz frequency only (Yang at al. 2018).

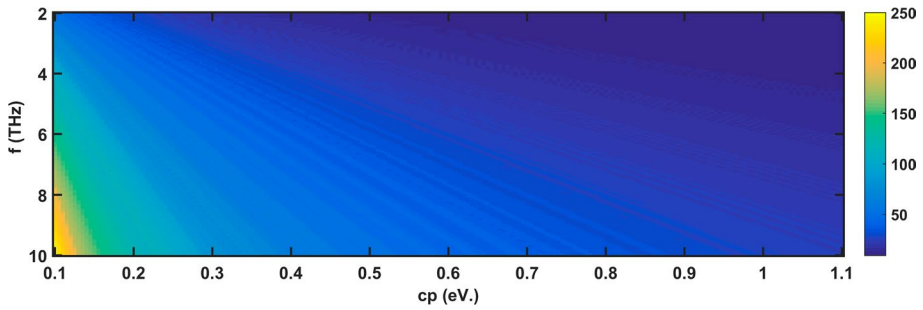


Fig. 3 Simulated 2D (E_f - ν) variation of FOM of the proposed gas sensor. The plot corresponds to FOM calculation while considering the gas RI values of 1 and 1.01

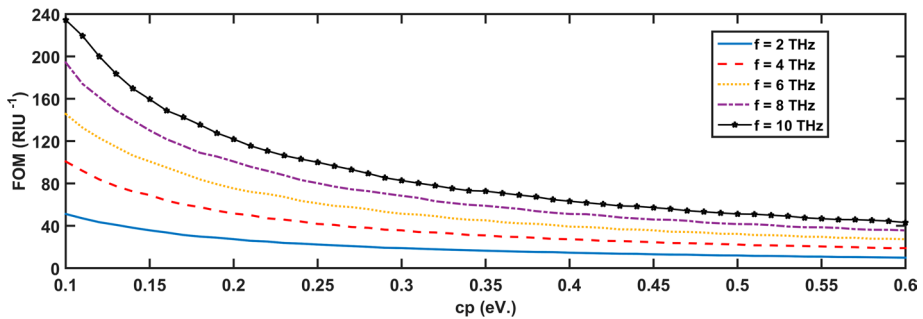


Fig. 4 Simulated variation of FOM with graphene’s chemical potential for five different THz frequencies. The plots correspond to FOM calculation while considering the gas RI values of 1 and 1.01

In this sequence, Fig. 4 presents the simpler and more categorical depiction of FOM variation with chemical potential at five different radiation frequencies ranging from 2 to 10 THz. Notably, the chemical potential range has been made limited to 0.6 eV (compared to 1.1 eV in Fig. 3). It is for the reason that chemical doping can permanently tune graphene for long-term device application assuming that once graphene is chemically prepared and doped (typical value of E_f around 0.6 eV), it is isolated from the environment (Aliofkhazraei et al. 2016; Mock 2012). Figure 4 clearly corroborates with Figs. 2 and 3, and emphasizes that moderate doping (smaller E_f) of graphene and higher THz frequency ($\cong 9$ –10 THz) lead to significantly greater FOM.

The major rationale behind this outcome is that the combination of smaller E_f and greater ν leads to sharper PSHE curve corresponding to any given value of n_a . This very fact is clearly evident from Fig. 2b, which exhibits significantly sharper (*i.e.*, with smaller FWHM) PSHE curves than those corresponding to Fig. 2a and c. For an entirely clear elaboration of the above argument, the following Table 1 enlists the values of S_a (deg./RIU), FWHM (deg.), and FOM (RIU⁻¹) corresponding to Figs. 2 a, b, and c.

The above table clearly indicates that the sensitivity remains nearly the same (in the vicinity of 13.5 deg./RIU) for all three combinations (of E_f and ν) and for whole range of n_a values. Considering the standard angular resolution of 0.001°, the calculated detection limit ($R_a = \frac{0.001}{S_a}$) comes out to be 7.41×10^{-5} RIU. However, there is a considerable variation in PSHE curve’s FWHM for different combinations of E_f and ν . Among three

Table 1 Simulated values of different sensing performance parameters (S_a , FWHM, and FOM) for three different combinations of ν and E_f : (a) $\nu=2$ THz and $E_f=0.1$ eV, (b) $\nu=10$ THz and $E_f=0.1$ eV, and (c) $\nu=10$ THz and $E_f=0.6$ eV

Parameter	Combination	$n_a = 1.01$	$n_a = 1.03$	$n_a = 1.05$	$n_a = 1.07$	$n_a = 1.1$
S_a	(a)	13.500	13.467	13.460	13.443	13.410
	(b)	13.500	13.467	13.440	13.428	13.400
	(c)	13.400	13.467	13.440	13.443	13.410
FWHM	(a)	0.269	0.284	0.301	0.317	0.343
	(b)	0.058	0.061	0.065	0.068	0.073
	(c)	0.321	0.339	0.358	0.377	0.407
FOM	(a)	50.186	47.418	44.712	42.407	39.096
	(b)	232.76	220.77	206.77	197.48	183.56
	(c)	41.75	39.73	37.54	35.66	32.95

combinations, the smallest FWHM values (*i.e.*, the sharpest PSHE curves) are achieved for smaller E_f and greater ν , which eventually leads to highest FOM. The corresponding minimum values of FWHM and maximum values of FOM are highlighted in the above table. From the above discussion, it can be explicitly established that a THz frequency in the vicinity of 9–10 THz and graphene’s chemical potential around 0.1 eV should be preferred in order to achieve significantly large FOM from the proposed PSHE-based gas sensor.

(iii) **Analysis of sensor’s performance for the range of gas RI values, and effect of temperature and magnetic field**

Figure 5 presents the variation of FOM with n_a at 10 THz frequency for different values of E_f .

Figure 5 demonstrates that for any value of E_f , the sensor’s FOM decreases for larger values of n_a . Focusing on the curve corresponding to $E_f=0.1$ eV (in view of the discussion in previous sections), it can be numerically appreciated that at $E_f=0.1$ eV (and $\nu=10$ THz), the FOM magnitude varies from its maximum value of 232.76 RIU⁻¹ (at $n_a=1$) to 183.56 RIU⁻¹ (at $n_a=1.1$), which tallies to nearly 20% decrease in FOM corresponding to n_a varying from 1 to 1.1. This decrease seems manageable as the FOM

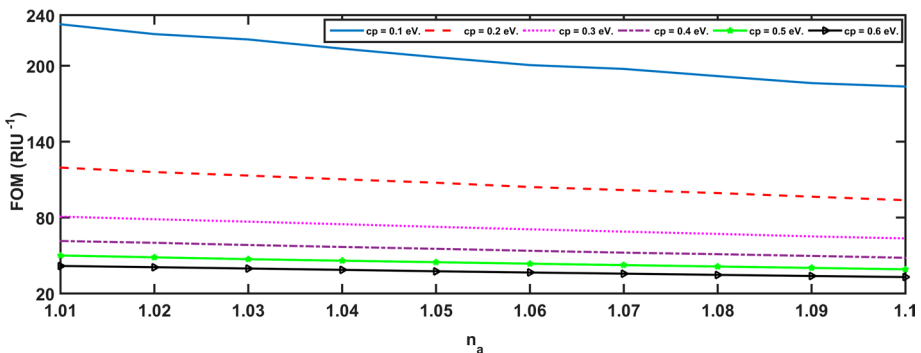


Fig. 5 Simulated variation of FOM with n_a at $\nu=10$ THz for different values of E_f . Here, $n_a=1$ has been taken as reference for FOM calculations

Table 2 Temperature-dependent FOM values of the proposed PSHE-based gas sensor at $\nu = 10$ THz and $E_r = 0.1$ eV. Two values of n_a are taken as 1 (reference: air) and 1.01 (analyte: gas)

S.N	Temperature (K)	FOM (RIU ⁻¹)
1	294	232.76
2	306	234.85
3	322	236.34
4	334	236.12
5	350	234.09

magnitudes corresponding to the above range of n_a are already large enough for highly sensitive and accurate measurement of n_a .

As a matter of fact, greater amount of FOM at smaller n_a values is an extremely vital outcome because in case of blend of gases, low n_a relates to smaller concentrations (*e.g.*, CO₂ in CH₄) (Giraudet 2016) and relatively larger FOM will surely cause more precise detection of low concentrations in gaseous mixtures. As another apparent application of this outcome may be in view of the reports that the fatal virus such as SARS-Cov-2 has an airborne transmission (Greenhalgh et al. 2021), probabilistically leading to extremely miniscule local variations in the air RI. The proposed sensor probe, with an appropriately-selected specificity material (*e.g.*, polyaniline, choline oxidase, polypyrrole, and glutamate oxidase etc.), may possibly be a useful instrument to deliver an early (due to graphene's prominent adsorption behavior) and accurate (due to large FOM at small RI) detection of SARS-Cov-2 infusion at the sites of expected high risk.

Further, it is very important to analyze the effect of temperature on the proposed sensor's performance. As discussed in Section-II, the thermo-optic effect in constituent media (Ge, organic layer, and graphene) is considered in the temperature range of 294 K–350 K. The following Table 2 enlists the values of FOM at 5 different temperatures in the above range.

The above table suggests that there is not much change in sensor's FOM when the temperature is varied. This is probably due to the reason that the variation in temperature does not change the PSHE curve's FWHM by any significant extent, and therefore, the FOM remains in the close vicinity of 235 RIU⁻¹. Hence, while assuming that the gas RI does not vary with temperature in the above range, it can be established that the influence of temperature on gas sensor's performance is negligible.

At THz, the imaginary part (absorption) of graphene monolayer increases with magnetic field (Zhang et al. 2017b), therefore, FWHM of the PSHE curve is bound to decrease with an increase in magnetic field (say, in a range of 0–1 T). It may fundamentally cause the PSHE spectrum to be deeper leading to smaller FWHM. On the other hand, the sensitivity tends to decrease with an increase in magnetic field. The FOM, in consequence, will increase with an increase in magnetic field.

(iv) A brief analysis of the sensor's performance with an alternative interrogation method

At this juncture, it should be noted here that the gas sensing with the proposed PSHE-based probe can also be performed in terms of an alternative method, *i.e.*, variation in SDS peak value upon change in gas medium RI. Under this method, the sensitivity (say, S_p) can be defined as:

Table 3 Simulated values of S_p for three different combinations of ν and E_f : (a) $\nu=2$ THz and $E_f=0.1$ eV, (b) $\nu=10$ THz and $E_f=0.1$ eV, and (c) $\nu=10$ THz and $E_f=0.6$ eV

Parameter	Combination	$n_a = 1.01$	$n_a = 1.03$	$n_a = 1.05$	$n_a = 1.07$	$n_a = 1.1$
S_p	(a)	2380.11	2336.68	2295.45	2255.40	2197.90
	(b)	1988.05	1981.28	1962.21	1918.95	1837.68
	(c)	365.21	378.07	375.28	370.32	362.05

$$S_p = \frac{(\delta_H^-)_{peak}}{\delta n_a} \tag{14}$$

From above expression, the unit of S_p is $\mu\text{m}/\text{RIU}$. Following Table 3 enlists some representative values of S_p ($\mu\text{m}/\text{RIU}$) corresponding to Fig. 2a, b, and c.

The above table indicates that for any given value of n_a , the combination of smaller values of both E_f and ν lead to greater S_p , which has been highlighted in the above table. There are two important aspects visible from the above table. First, an increase in E_f leads to decrease in S_p , which is consistent with the outcomes discussed in earlier sections. Second, for small E_f (0.1 eV here), S_p has an inverse dependence on ν , *i.e.*, the smaller the THz frequency, the greater is the magnitude of S_p . This is an extremely important result as it not only opens up an alternative method to carry out the sensing procedure but it also provides a huge flexibility to the sensor design in terms of selecting the THz frequency. More precisely, if a smaller THz frequency source is available, then one may opt for this method (*i.e.*, measuring the variation in SDS peak value of PSHE spectrum upon change in gas medium RI), and for greater THz frequency source, one can use the angular form of the PSHE spectrum (as discussed in previous sections). Nonetheless, in either of the methods, the value of E_f should be chosen in the vicinity of 0.1 eV.

4 Conclusions

PSHE-based plasmonic sensor with Ge prism, thick organic layer, and graphene is simulated and analyzed in THz region for gas sensing. The results suggest that with angular interrogation method, significantly larger FOM ($\sim 235 \text{ RIU}^{-1}$) for gaseous sensing can be achieved with smaller chemical potential (*e.g.*, 0.1 eV) and higher THz radiation frequency (*e.g.*, 9–10 THz). Further, the sensor’s FOM increases for smaller refractive index of gaseous media. This very feature may possibly be relevant in early detection of airborne viruses (*e.g.*, SARS-COV-2) and detection of small concentrations in gaseous mixtures (*e.g.*, CO_2 in CH_4). Moreover, the influence of temperature on gas sensor’s performance (FOM) is negligible, which suggests that the sensor is capable of providing stable sensing performance against temperature variation. As a crucial addition to the sensor design flexibility, the probe can still be operated at a smaller THz frequency (*e.g.*, 2 THz) by following an alternative interrogation scheme (*i.e.*, measuring the variation in SDS peak value of PSHE spectrum upon change in gas medium RI). Interestingly, other 2D materials such as black phosphorus (BP) and transition metal dichalcogenides (TMD) can also provide extremely efficient manipulation of the propagation and detection of THz waves (Shi et al. 2018).

The study of PSHE-based plasmonic sensor with BP and TMDs can be a part of our future research on this theme.

Supplementary Information The online version contains supplementary material available at <https://doi.org/10.1007/s11082-022-03626-7>.

Acknowledgements Anuj K. Sharma (Principal Investigator), Y. K. Prajapati (Co- Principal Investigator), and P. Kumar (Research staff) gratefully acknowledge the core research grant (Project no.: CRG/2019/002636) from Science and Engineering Research Board (SERB) India that fully funded this research work.

Funding This work was fully funded by the core research grant (CRG/2019/002636) sponsored by the Science and Engineering Research Board (SERB) India. Please see the Acknowledgments section for specific roles of the authors in this research grant.

Declarations

Conflict of interest The authors declare no conflict of interest.

References

- Aiello, A., Woerdman, J.P.: Role of beam propagation in Goos-Hänchen and Imbert-Fedorov shifts. *Opt. Lett.* **33**(13), 1437 (2008)
- Aliofkhaei, M., et al.: *Graphene Science Handbook: Electrical and optical properties*. CRC Press, Boca Raton (2016)
- Bao, Q., Loh, K.P.: Graphene photonics, plasmonics, and broadband optoelectronic devices. *ACS Nano* **6**, 3677–3694 (2012)
- Barlow, H., Cullen, A.: Surface waves. *Proc. IEE III: Radio Commun. Eng.* **100**(68), 329 (1953)
- Bliokh, K.Y., Bliokh, Y.P.: Topological spin transport of photons : the optical Magnus effect and Berry phase. *Phys. Lett. A* **333**(3–4), 181–186 (2004)
- Bliokh, K.Y., et al.: Spin-orbit interactions of light. *Nat. Photonics* **9**(12), 796–808 (2015)
- Boucaud, P., et al.: Nanocrystalline diamond photonics platform with high quality factor photonic crystal cavities. *App. Phys. Lett.* **171115**(2012), 1–5 (2014)
- Filonov, D.S., et al.: Photonic spin Hall effect in hyperbolic metamaterials for polarization-controlled routing of subwavelength modes. *Nat. Commun.* **5**(1), 3216 (2014)
- Gan, C.H., Chu, H.S., Li, E.P.: Synthesis of highly confined surface plasmon modes with doped graphene sheets in the midinfrared and terahertz frequencies. *Phys. Rev. B* **85**(12), 125431 (2012)
- Gan, C.H., Analysis of surface plasmon excitation at terahertz frequencies with highly doped graphene sheets via attenuated total reflection. *Appl. Phys. Lett.* **101** (2012)
- Giraudet, C., et al.: Concentration dependent RI of CO₂/CH₄ mixture in gaseous and supercritical phases. *J. Chem. Phys.* **144**, 134304 (2016)
- Gosselin, P., Be A. (2007) Spin Hall effect of photons in a static gravitational field, 75(8): 1–6
- Greenhalgh, T., et al.: Ten scientific reasons in support of airborne transmission of SARS-COV-2. *Lancet* **397**, 1603–1605 (2021)
- Hetch, E.: *Optics*. Addison-Wesley, Boston (2002)
- Hibbins, A.P., Benjamin, R.E., Sambles, J.R.: Experimental verification of designer surface plasmons. *Science* **308**(5722), 670–672 (2005)
- Hirsch, J.E.: Spin hall effect. *Phys. Rev. Lett.* **83**(9), 1834–1837 (1999)
- Jabbarzadeh, F., Heydari, M., Habibzadeh-Sharif, A.: A comparative analysis of the accuracy of Kubo formulations for graphene plasmonics. *Mater. Res. Express* **6**(8), 086209 (2019)
- Kato, Y.K., et al.: Observation of the spin hall in semiconductor. *Science* **306**(1910), 1–5 (2004)
- Koppens, F.H.L., Chang, D.E., García de Abajo, F.J.: Graphene plasmonics: a platform for strong light-matter interactions. *Nano Letters* **11**(8), 3370–3377 (2011)
- Kumar, S., et al.: MoS₂ functionalized multicore fiber probes for selective detection of Shigella bacteria based on localized plasmon. *J. Lightwave. Technol.* **39**(12), 4069–4081 (2021)

- Li, Y., et al.: One-dimensional multiband terahertz graphene photonic crystal filters. *Opt. Mat. Exp.* **7**(4), 1228 (2017)
- Ling, X., et al.: Steering far-field spin-dependent splitting of light by inhomogeneous anisotropic media. *Phys. Rev. A* **86**(5), 1–5 (2012)
- Ling, X., et al.: Recent advances in the spin Hall effect of light. *Rep. Prog. Phys.* **80**(6), 066401 (2017)
- Liu, Y.L., et al.: Magneto-optical effects on the properties of the photonic spin Hall effect owing to the defect mode in photonic crystals with plasma. *AIP Adv.* **9**(7), 075111 (2019)
- Lobry, M., et al.: HER2 biosensing through SPR-envelope tracking in plasmonic optical fiber gratings. *Biomed. Opt. Exp.* **11**(9), 4862–4871 (2020)
- Lockyear, M.J., Hibbins, A.P., Sambles, J.R.: Microwave surface-plasmon-like modes on thin metamaterials. *Phys. Rev. Lett.* **102**(7), 073901 (2009)
- Mock, A.: Padé approximant spectral fit for FDTD simulation of graphene in the near infrared. *Opt. Mater. Exp.* **2**(6), 771–781 (2012)
- Murakami, S., Nagaosa, N., Zhang, S.: Dissipationless Quantum Spin. *Science* **301**, 1348–1351 (2003)
- Naftaly, M., Chick, S., Matmon, G., Murrin, B.: Refractive Indices of Ge and Si at Temperatures between 4–296 K in the 4–8 THz Region. *Appl. Sci.* **11**(2), 487 (2021)
- Novoselov, K.S., Geim, A.K., Morozov, S.V., Jiang, D.-E., Yanshui, Z., Dubonos, S.V., Grigorieva, I.V., Firsov, A.A.: Electric field effect in atomically thin carbon films. *Science* **306**(5696), 666–669 (2004)
- Otto, A.: Excitation of nonradiative surface plasma waves in silver by method of frustrated total reflection. *Z. Phys.* **216**(4), 398–410 (1968)
- Pendry, J.B., Martín-Moreno, L.L., Garcia-Vidal, F.J.: Mimicking surface plasmons with structured surfaces. *Science* **305**, 847 (2004)
- Pinto, H., Markevich, A.: Electronic and electrochemical doping of graphene by surface absorbates. *Beilstein J. Nanotechnol.* **5**, 1842–1848 (2014)
- Prajapati, Y.K.: Photonic spin Hall effect detection using weak measurement in the SPR structure using antimoney: a sensing application. *Superlat. Microstruct.* **155**, 106886 (2021)
- Rizal, C.: Magneto-optic-plasmonic sensors with improved performance. *IEEE Trans. Magnet.* **57**(2), 1–5 (2021)
- Sharma, A.K., Nagao, T.: Design of a silicon-based plasmonic optical sensor for magnetic field monitoring in the infrared. *App. Phys. B.* **117**, 363–368 (2014)
- Shi, J., et al.: THz photonics in two dimensional materials and metamaterials: properties, devices, and prospects. *J. Mat. Chem. C* **6**, 1291–1306 (2018)
- Srivastava, T., et al.: Graphene based surface plasmon resonance gas sensor for terahertz. *Opt. Quant. Electron.* **48**(6), 1–11 (2016)
- Srivastava, A., Sharma, A.K., Prajapati, Y.K.: On the sensitivity-enhancement in plasmonic biosensor with photonic spin Hall effect at visible wavelength. *Chem. Phys. Lett.* **774**, 138613 (2021)
- Tan, X., Zhu, X.: Enhancing photonic spin Hall effect via long-range surface plasmon resonance. *Opt. Lett.* **41**(11), 2478–2481 (2016)
- Ulrich, R., Tacke, M.: Submillimeter waveguiding on periodic metal structure. *Appl. Phys. Lett.* **22**, 251 (1973)
- Xiang, Y., et al.: Enhanced spin Hall effect of reflected light with guided-wave surface plasmon resonance. *Photon. Res.* **5**(5), 467 (2017)
- Yang, L., et al.: Toxic chemical compound detection by terahertz spectroscopy: a review. *Rev. Anal. Chem.* **37**(3), 1–10 (2018)
- Yao, H., Zhong, S.: High-mode spoof SPP of periodic metal grooves for ultra-sensitive terahertz sensing. *Opt. Express* **22**(21), 25149–25160 (2014)
- Z. Zhang et al., “Graphene based surface plasmon resonance gas sensor with magnetic field control for terahertz,” *Prog. Electrom. Res. Symp.*, Nov. 19–22, 2017a.
- Z. Zhang et al., “Graphene based surface plasmon resonance gas sensor with magnetic field control for terahertz,” *Prog. Electron. Res. Symp.*, pp. 19–22, 2017b.
- Zhou, X., et al.: Identifying graphene layers via spin Hall effect of light. *App. Phys. Lett.* **101**, 251602 (2012)
- Zhou, X., et al.: Observation of Spin Hall Effect in Photon tunneling via weak measurements. *Sci. Rep.* **4**, 7388 (2014)